J. dynamic behavior mater. (2017) 3:12–22
DOI 10.1007/s40870-016-0090-2

Application of the Virtual Fields Method to Rubbers Under Medium Strain Rate Deformation Using Both Acceleration and Traction Force Data

Sung-Ho Yoon[1] · **Clive R. Siviour**[1]

Received: 30 October 2016 / Accepted: 26 December 2016 / Published online: 13 February 2017

Abstract This paper describes an experimental technique for characterizing the uniaxial stress–strain relationship of rubbers under medium strain rate deformation. This method combines the virtual fields method (VFM) and high-speed imaging with digital image correlation. The VFM can be expressed so that force measurement during dynamic loading is no longer required; instead, surface measurements of acceleration, which occurs as a result of wave propagation in the specimen, are used as a 'virtual load cell'. In a previous paper, the authors have utilized this technique for characterizing material parameters for the dynamic behaviour of rubbers using a drop-weight apparatus. One limitation of this technique is that the stability of the parameter estimation depends on the length of the specimen. When the loading stress wave reaches the fixed end of the specimen, a static equilibrium state is instantaneously achieved. At this instant, the acceleration fields are no longer able to provide information, and the identification is unstable. In order to overcome this limitation, the present paper proposes a VFM based method able to produce stable identification even at this equilibrium instant. This procedure utilizes both inertial and external forces, and a new experiment apparatus has been developed for simultaneously measuring these two sets of data. This new procedure is described using results from simulations; then, the experimental system and results will be presented.

Keywords Elastomers · High-strain rate · Mechanical characterization · Virtual fields method · Inverse method

✉ Clive R. Siviour
clive.siviour@eng.ox.ac.uk

[1] Department of Engineering Science, University of Oxford, Parks Road, Oxford OX1 3PJ, UK

Introduction

Rubbers are used in many engineering applications, in fields ranging from consumer products to aerospace to military. One of the useful characteristics of rubbers is dissipation of mechanical energy, allowing the material to be used for energy absorption, which is of particular interest for impact protection. For example, one application is elastomeric coatings on concrete masonry unit walls; elastomers are also used to protect mobile devices such as cell phones. When rubbers are used in such applications, the strain rate induced by impact loading can fall into the so-called dynamic range ($1–10^4$ s^{-1}) [1]. For example, the strain rate experienced by a rubber protective layer on masonry walls can reach the order of 100 s^{-1} [2]. However, the mechanical behaviour of rubbers is very sensitive to deformation rate even between quasi-static rates (10^{-4}–1 s^{-1}) [3]. Understating the dynamic and rate dependent behaviour is therefore important, not only to achieve cost-effective use of the materials but also ensure a targeted safety level. These two aspects can be achieved by appropriate engineering design, but engineering design cannot be reliable unless material behaviour in the service conditions is well understood. Thus, it is clear that the mechanical characterization of rubbers over a wide range of strain rates is essential.

The most widely used test method for mechanical characterizations of materials at dynamic strain rates is the split Hopkinson bar. This technique has been used for characterizing the dynamic stress–strain curve of rubbers in compression [3–5]. Alternative dynamic techniques, based on a modified Charpy tester, commercial hydraulic load frame and gas gun have also been developed for testing rubbers in tension [6–8]. Although many efforts have been made in the design and performance of these tests, there are several experimental difficulties due to the low Young's modulus of rubbers. The

first difficulty is low signal-to-noise ratio of force measurements during dynamic loading. This difficulty is typically expected when the split Hopkinson pressure bar (SHPB) experiment is conducted with high impedance metallic bars on a low impedance rubber specimen [9]. The second limitation is the achievement of static stress equilibrium in the dynamic experiment. This limitation needs to be considered for all Hopkinson bar type dynamic experiments, in which remote measurement of specimen behaviour are made, but it is more difficult for rubbers to obtain this equilibrium state within the initial loading period due to their low wave speed [10]. Thus, the force data measured from one end of a specimen will differ from that at the other end, and these measurements are affected by both specimen and material response, rather than measuring material response alone.

Recently, the authors have developed an entirely different approach [11]. The new method is based on the combination of two modern experimental techniques: full-field measurement supported by high-speed imaging and digital image correlation [12], and the Virtual Fields Method (VFM) [13]. The VFM is an inverse method by which material constitutive parameters are inversely characterized by applying experimental observations such as strain and force data to the principle of virtual work equation. This equation is written as

$$-\int_{\mathrm{v}} \sigma{:}\varepsilon^{*} d\mathrm{v} + \int_{s_f} T \cdot u^{*} ds = \int_{\mathrm{v}} \rho a \cdot u^{*} d\mathrm{v} \tag{1}$$

where, $\boldsymbol{\sigma}$ is actual stress tensor, $\boldsymbol{T}$ actual loading ($=\boldsymbol{\sigma n}$), $\boldsymbol{u}^{*}$ virtual displacement vector, $\boldsymbol{a}$ acceleration, $\boldsymbol{\varepsilon}^{*}$ virtual strain tensor ($=\partial \boldsymbol{u}^{*}/\partial \boldsymbol{x}$), v current volume of the body, s_f current loaded surface, ':' and '·' the dot products for matrices and vectors.

For a quasi-static experiment, the inertial force term (the right-hand side of Eq. (1)) is negligible and can be omitted. When materials are dynamically loaded, this inertial term becomes significant due to the high accelerations, causing a non-uniform deformation of a test sample. Several previous works have modified this equation to remove the traction force term (the second term of the left-hand side of Eq. (1)) by applying appropriate virtual fields [14], for example,

$$\begin{cases} u_x^{*(1)} = x(x-L) \\ u_y^{*(1)} = 0 \end{cases} \Rightarrow \begin{cases} \varepsilon_x^{*(1)} = 2x - L \\ \varepsilon_y^{*(1)} = 0 \\ \varepsilon_{xy}^{*(1)} = 0 \end{cases}$$
$$\begin{cases} u_x^{*(2)} = 0 \\ u_y^{*(2)} = x(x-L)y \end{cases} \Rightarrow \begin{cases} \varepsilon_x^{*(2)} = 0 \\ \varepsilon_y^{*(2)} = x(x-L) \\ \varepsilon_{xy}^{*(2)} = (2x-L)y \end{cases} \tag{2}$$

where x and y are the axial and transverse coordinates and L indicates the axial distance from the fixed to loaded boundary. With these virtual fields, Eq. (1) can be rewritten as

$$-\int_{\mathrm{v}} \sigma{:}\varepsilon^{*} d\mathrm{v} = \int_{\mathrm{v}} \rho a \cdot u^{*} d\mathrm{v} \tag{3}$$

The cancellation of the traction force term in Eq. (1) means that the force measurement during dynamic loading is not required; instead the inertial force term is utilized as load cell. The fact that the traditional force measurement is not required is a significant advantage for a dynamic test on rubbers since the aforementioned experimental difficulties in terms of force measurement do not need to be considered. The application of this equation can be referred to as the dynamic VFM and has been adopted for characterizing various materials such as metal [15, 16], composites [14, 17] and concrete [18]. The present author used Eq. (3) to identify the Young's modulus of a silicone rubber under a small amplitude dynamic loading, in tension, produced by a drop-weight apparatus; the identification and experimental procedure is described in a previous paper [11]. The Young's modulus identification is conducted with different pre-stretching levels imposed on the rubber specimen. A series of Young's moduli (averaged values from each test) is collected and used in a special optimization with the assumption that each modulus is a tangent to the actual stress–strain curve of the test specimen; numerical simulation and experimental data showed that this assumption yields reasonable characterisation of material properties. A suitable hyperelastic model is assumed in this optimization procedure, and the unknown model parameters are obtained. The drop-weight apparatus is schematically described in Fig. 1.

However, this technique does have a limitation. To demonstrate this, experiments have been performed on silicone (Sylgard 184 silicone elastomer, Dow Corning)

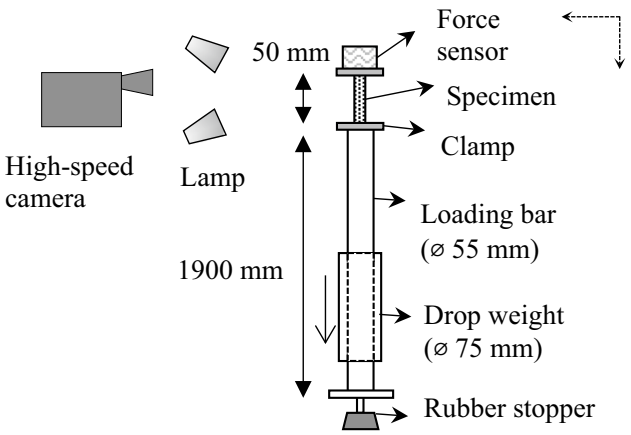

Fig. 1 Schematic diagram of the drop-weight dynamic test

and nitrile rubbers (Coru118, Coruba). Uniaxial type specimens were prepared from these two rubber sheets with dimensions of width = 13 mm and length = 80 mm. The thickness is uniformly about 1 mm. After inserting the specimens between the two clamps in the drop-weight apparatus, as shown in Fig. 1, the gauge length is approximately 50 mm. The dynamic experiment was identically conducted as presented in the previous work [11]; the procedure is briefly described again here. First, the specimen is located on top of the drop-weight apparatus. The ends of the specimen are clamped by the two fixtures. The cylindrical weight is manually dropped from a certain location; when the end of the loading bar is impacted by the weight, the tensile loading wave travels toward the specimen. The bottom clamp is displaced downward and hence the rubber specimen is dynamically stretched. At this instant, a high-speed camera (FASTCAM SA 5, Photron) is triggered in order to capture the dynamic deformations at an imaging speed of 50 000 fps. Each digital image taken by this camera is analysed by means of a commercial digital image correlation package (Davis 7.2, LaVision 2007). From this analysis, the strain and acceleration data fields are obtained at each imaging time step. These data are applied to Eq. (3) in which the stress term $\boldsymbol{\sigma}$ is described by the linear elastic constitutive model with the two unknown parameters: Young's modulus E and Poisson' ratio ν. Equation (3) can then be rewritten in the form of a system of linear equations. Evaluation of these equations leads to the identification of E and ν at each time step. The identification results for the silicone and nitrile rubber are given in Fig. 2.

The identification period shown in Fig. 2 is approximately the initial incident loading period, after which a slight unloading period occurs due to wave reflection within the loading bar. Within this initial loading period, there is at least one wave reflection in the specimen; that is, the stress wave reaches the fixed end of the specimen. According to the observation of the strain data field, the stress wave reached the fixed end at about 0.5 and 0.7 ms for the case of the silicone and nitrile rubbers, respectively. At a similar instant, it can be seen that the Young's modulus identification falls below zero before returning to positive values. The reason for this unstable identification is that static stress equilibrium is achieved for a short period when the stress wave reaches the fixed end. During this temporary equilibrium state, the inertial force term of Eq. (3) is close to zero; this means that no force data exist in the principle of virtual work equation.

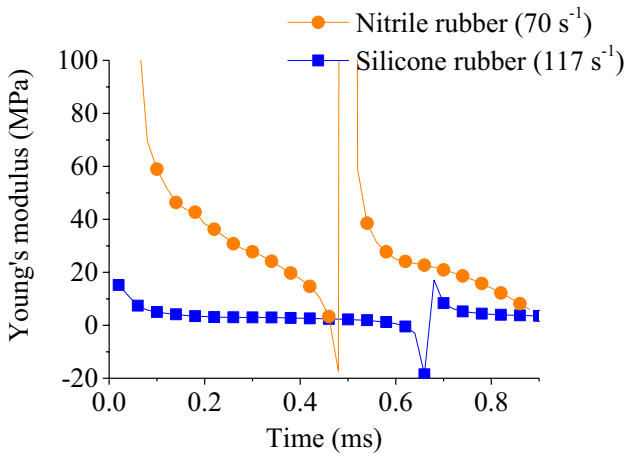

Fig. 2 Young's modulus identifications from the VFM application to the drop-weight experiment

In the previous work, the averaged Young's moduli were obtained from identification results at different prestretch levels in order conduct an optimization procedure allowing the constitutive parameters of the assumed hyperelastic model to be calculated. For example, the averaged value for the silicone rubber can be calculated using the Young's modulus from 0.2 to 0.5 ms, over which time the identifications are stable. The method used to determine the stable identification period is to consider the assumption that rubbers should exhibit rate independent compressibility, so that the Poisson's ratio, identified during the averaging period, should be close to that obtained from a quasi-static test. This method works well for determining the starting point of the averaging period. However, the unstable identification of the Poisson's ratio during the temporary equilibrium state is not as significant as that of the Young's modulus. Thus, it is not clear when to define the final point. This problem can significantly affect the identification result of the averaged Young's modulus, especially when rubbers exhibit a large amount of stress relaxation; this is evident in Fig. 2 in that the identification result from the nitrile rubber decreases more than that of the silicone rubber during the identification period. For this case, the averaged Young's modulus is greatly influenced by the length of the averaging period. Furthermore, if the rubber specimen is shorter or stiffer, the unstable identification moment occurs earlier so that the determination of the averaging period can be more difficult and its significance on the averaged modulus can be higher.

In the present paper, a new VFM and experimental procedure is proposed in order to overcome the experimental limitation of the current dynamic VFM technique on rubbers. The next section will describe this new VFM procedure using a finite element simulation that resembles the new experimental conditions, and explain how to remove the unstable identification moment and extend the stable identification period. The next section also explains an alternative way to reconstruct the stress–strain curve

without using the optimization procedure introduced in the previous work [11].

Simulation

Finite Element simulation studies were conducted using ABAQUS. A two-dimensional rectangular specimen was designed with similar dimensions as used in the actual experiment. The geometry is schematically described in Fig. 3 left). The left-hand boundary is fixed, and the velocity boundary condition (Fig. 3 right), which was obtained from the actual experiment, is imposed on the right-hand side boundary. The fixed boundary condition in the y direction is applied on both ends. ABAQUS/explicit simulations were performed with a CPS4R (four-node plane stress, reduced integration) element type and the maximum calculation time increment of 1 μs. The element size was chosen as 0.5 mm. The same simulation procedure is described more in detail in the previous work [11]. For the material model, the two-term Ogden [19] and linear viscoelastic models (Prony series) are adopted to simulate the rate-dependent hyperelastic behaviour. The parameters for the Ogden mode were obtained from a quasi-static uniaxial test (0.01 s^{-1}) on the same nitrile rubber. The dynamic mechanical analysis (DMA) with the aid of time–temperature superposition was used to obtain the relaxation curve of the same material, which was then fitted to the Prony series in order to obtain the parameters for the viscoelastic part. The same description of the quasi-static experiment and DMA application can be found in the previous work [11]. The material parameters are listed in Table 1. It should be noted that for the hyperelastic model a large bulk modulus (K = 400 MPa) is given to simulate an almost incompressible behaviour.

The strain and acceleration data fields were extracted, using the method as in the previous work [11], from the simulation result at a time interval of 0.02 ms, which is the same interval as the imaging speed, 50 000 fps, in the experiment. The extracted data fields were applied to the principle of virtual work equation, Eqs. (2 and 3), in order to obtain the Young's modulus identifications at each time step. The identification result from Eq. (3) is referred to as the Old VFM from this section onwards.

The role of the first virtual field of Eq. (2) is to impose zero (axial) virtual displacements on both ends of the

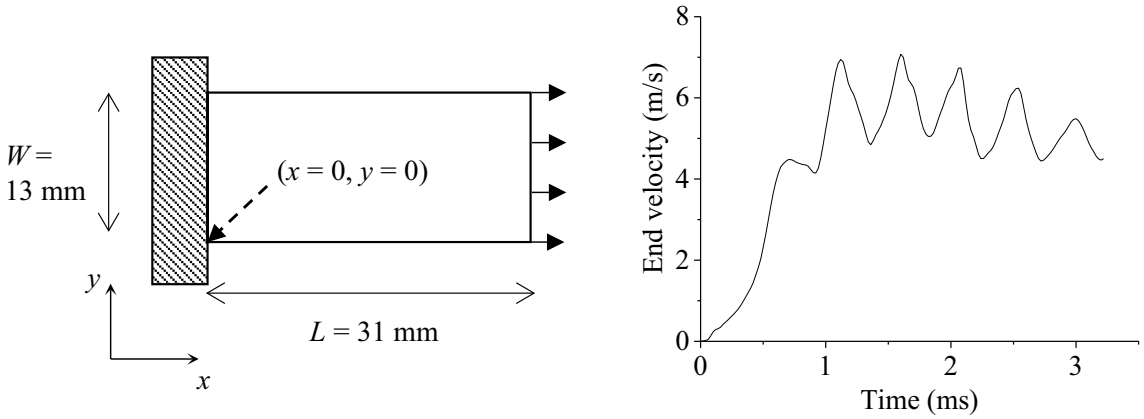

Fig. 3 *Left* two dimensional simulation geometry (the hatched *rectangle* represents the fixed boundary condition and the *solid arrows* on the *right*-hand side boundary indicates the velocity boundary condition); *right* the velocity profile imposed on the right-hand side boundary

Table 1 Simulation parameters for the two-term Ogden and Prony series models: $\log(\tau_i)$ and g_i are respectively logarithmic relaxation time and normalized shear modulus terms

Two-term Ogden											
μ_1 (MPa)	α_1	μ_2 (MPa)	α_1								
0.028	0.004	0.014	0.014								
Prony series											
$\log(\tau_i)$	−19	−18	−17	−16	−15	−14	−13	−12	−11	−10	−9
g_i	0.028	0.004	0.014	0.014	0.024	0.020	0.046	0.047	0.149	0.027	0.201
$\log(\tau_i)$	−8	−7	−6	−5	−4	−3	−2	−1	0		
g_i	0.156	0.198	0.056	0.010	0.003	0.001	0.001	0.0002	0.001		

specimen: the term x and $(x - L)$ respectively are null at the left- and right-hand side ends so that the tractions from both ends can be cancelled from the principle of virtual work equation. If the virtual fields can cancel the contribution of the traction over the fixed boundary, it is referred to as the kinematically admissible (KA) virtual field [13]. The principle of virtual work equation, Eq. (1), is only valid when such a KA virtual field is applied. However, a non-KA virtual field can be also used if the traction from the fixed boundary is known. In the current case, it is assumed that in the experiment we can measure the traction of the fixed boundary during the dynamic loading. This assumption allows the removal of the term x from Eq. (2). The term $(x – L)$ remains to cancel the traction from the loaded boundary, because it can be difficult to measure the reaction force from a dynamically loaded boundary. With this assumption, the first virtual field is rewritten as

$$\begin{cases} u_x^{*(1)} = (x - L) \\ u_y^{*(1)} = 0 \end{cases} \Rightarrow \begin{cases} \varepsilon_x^{*(1)} = 1 \\ \varepsilon_y^{*(1)} = 0 \\ \varepsilon_{xy}^{*(1)} = 0 \end{cases} \tag{4}$$

The second virtual field remains the same to be KA for cancelling any lateral traction contribution which is experimentally difficult to measure. With this new virtual field, the principle of virtual equation is written as

$$-\int_{\mathrm{v}} \sigma{:}\varepsilon^* d\mathrm{v} + \int_{s_u} T \cdot u^* ds = \int_{\mathrm{v}} \rho a \cdot u^* d\mathrm{v} \tag{5}$$

where s_u indicates the fixed boundary. The same simulation data fields were applied to this new equation. For the virtual work term of the traction force, the reaction force data were extracted from the nodes over the fixed boundary to supply the axial traction, $\boldsymbol{T}_x$.

The identifications of the Young's modulus from the Old and New VFMs are given in Fig. 4. The black solid line represents the identification history from the Old VFM, in which the unstable identification instants can be observed as similarly shown in the preliminary experimental result in Fig. 2. The stable identification period between these instants becomes shorter with increasing time during the loading. This reduction could be due to not only the temporary equilibrium state, but also the complex loading history as shown in Fig. 3 right. In contrast, the result (red line) from the New VFM shows a very stable identification for the whole loading period. No unstable identification instant is found, except for the very early loading period, although there are multiple wave reflections within the specimen. The two identification results are almost coincident during the initial loading period ($t < 1$ ms). Thus, the old method to obtain the averaged Young's modulus can work for this period. However, after this period, the result from the Old VFM significantly deviates from that of the new method;

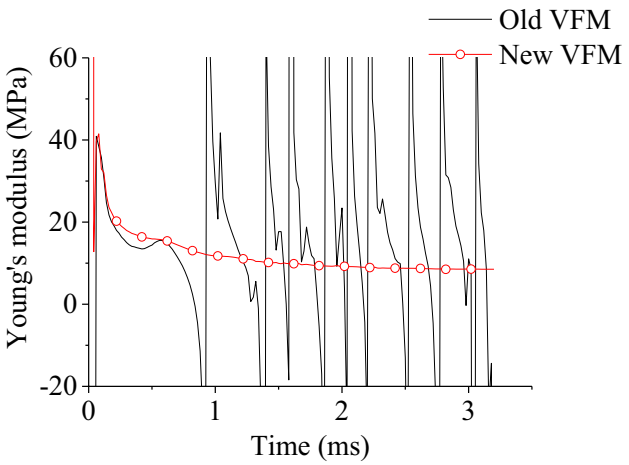

Fig. 4 Young's modulus identification results obatained from the old (Eq. (2)) and new (Eq. (5)) VFMs applied to Nitrile Rubber

the stable identification period becomes shorter and, so, only for short periods of time the two results are coincident.

In the previous work [11], the averaged Young's modulus obtained during the initial loading period is assumed to be a tangent slope of the actual stress–strain curve. This assumption was made because the strain amplitude during this initial loading period is relatively small ($\varepsilon < 0.05$), so static pre-stretching was used to obtain data at larger strains. The identification result of the New VFM can be also used to obtain the averaged modulus within a small strain amplitude loading period. Then, each averaged modulus obtained from the dynamic test with different pre-stretching levels can be applied to the optimization procedure with an assumed hyperelastic model in order to find the optimized material parameters.

One limitation of this method is that a hyperelastic model needs to be assumed prior to knowing the actual stress–strain behaviour. With regard to this limitation, the new approach can be applied to the new identification result to reconstruct the stress–strain curve without assuming any particular model. This new approach is allowed by the fact that the new identification result is stable for a long loading period (i.e. large deformation). With this advantage, the axial stress is simply calculated by multiplying the spatially averaged axial true strain at each time step to the corresponding Young's modulus. This can be mathematically expressed as

$$\sigma_x(t) = E_{VFM}(t) \times \bar{\varepsilon}_x(t) \tag{5}$$

where the overbar of ε indicates a spatially averaged value. This equation is used to reconstruct the true stress–strain curve during the whole dynamic loading period. The reconstructed curve (red line) is given in Fig. 5. For comparison, the stress–strain curve directly extracted from an element

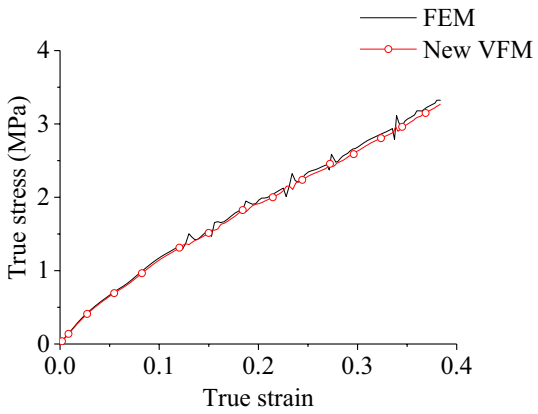

Fig. 5 Comparison with the true stress–strain curves obtained from the New VFM and extracted from the simulation

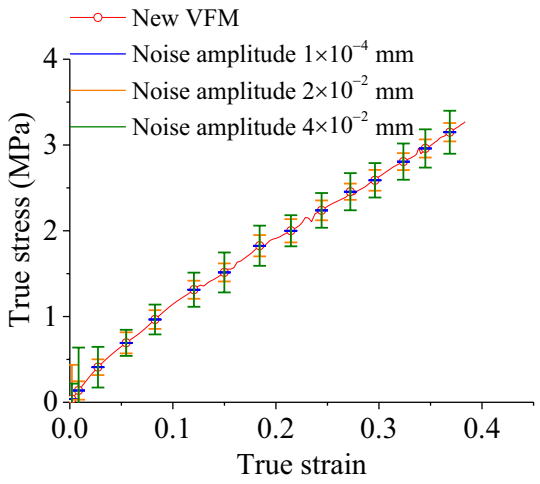

Fig. 6 True stress–strain curve from the New VFM and error bars indicating the effect of adding noise to the simulation data

in the FEM simulation is given as a black solid line. The stress–strain curve from the simulation is obtained by averaging the stress and strain values at each time step. The comparison shows that the reconstructed curve from the New VFM is well matched with the given behaviour of the simulation. This result means that the constitutive model assumption is not required to reconstruct a nonlinear stress–strain curve when the identification result of the New VFM is used with the simple reconstruction approach of Eq. (5).

White Gaussian noise was then added to the raw displacement data in order to evaluate the sensitivity of the stress–strain curve of the New VFM with respect to noise in the imaging system. Random noise was added to the displacement data directly extracted from the simulation output. The overall procedure of this noise addition is described in detail in the previous work [11]. There are three different noise amplitudes: 1×10^{-4}, 2×10^{-2} and 4×10^{-2} mm. The polluted displacement data were then numerically differentiated to generate the corresponding strain and acceleration data fields. These two data sets were used for the procedure of the New VFM as described above. The true stress–strain curve from Fig. 5 is replotted in Fig. 6, together with error bars obtained from the polluted data. The smallest and largest noise amplitudes make respectively about 0.01 and 6% deviation with respect to the raw stress–strain curve. The amplitude of random noise in the experiment can be obtained by using still images [16]. In the present experimental work, 30 still images of a sample were taken (a typical sample in a dynamic experiment is presented on the right hand side of Fig. 7) with the same imaging configuration as the one used for the actual test. The same configuration of digital image correlation as used in the actual analysis was applied to the still pictures, and the averaged noise amplitudes (standard deviation) are obtained as 4×10^{-4} mm and 3×10^{-4} mm respectively for the loading and transverse directions. The expected deviation, owing to this noise, of the stress–strain curve obtained from the present method therefore has magnitude 0.01%.

Experiment

Experimental Data and Analysis: Loading Only

The New VFM procedure was identically applied to data from a dynamic experiment using a new apparatus which produced the boundary condition given in Fig. 3 right. This new experimental system was developed with the requirements to produce a longer deformation amplitude than that of the drop-weight apparatus introduced in the previous work [11] and to provide force measurement during the dynamic loading. The new experimental system satisfying these two requirements is described in Fig. 7 and consists of three parts: incident bar, specimen clamps and impacting bar. The impacting bar travels at 6–8 m s^{-1} in the direction indicated by the arrow. The bar passes through the metal plate attached to the end of the gas-gun barrel. Next to the end of the gun barrel, a uniaxial piezoelectric force sensor (PCB Piezotronics, 208C02) is attached to the metal plate. The other side of the force sensor is connected to the clamp, which is used to apply the fixed boundary condition on one end of the uniaxial type rubber specimen. The other end of the specimen is attached to the other clamp which is connected to the end of the incident bar. The incident bar is dynamically displaced by the impact of the impacting bar on the middle of the clamp. In order to remove high frequency oscillation, two EPDM rubber layers (thickness = 2 mm) are attached at the location of impact. The

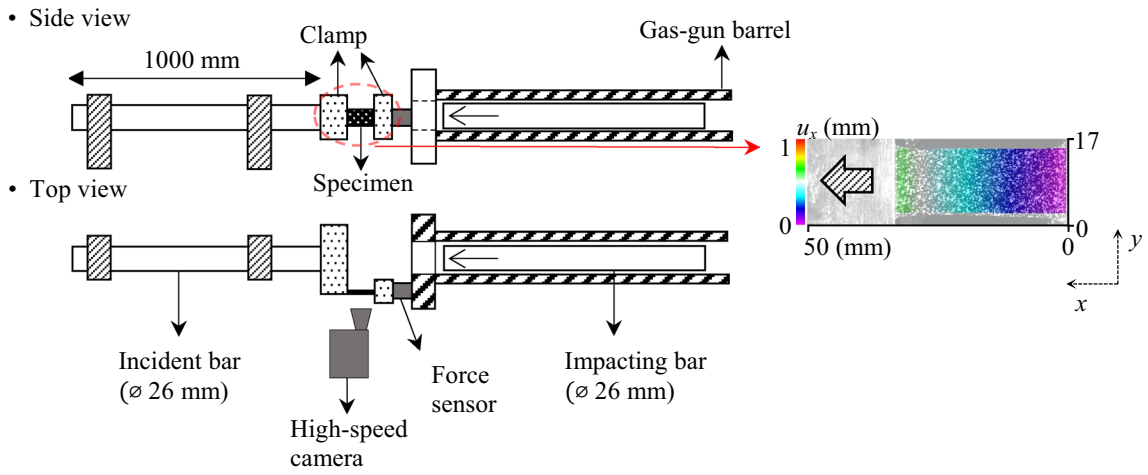

Fig. 7 Schematic representation of the dynamic tension test on a rubber sheet; the picture on the right-hand side shows one of the dynamic displacement fields in the axial direction, which is overlaid on an actual picture of the specimen

Table 2 Imaging and DIC analysis configurations

Camera	FASTCAM SA 5, photron
DIC software	Davis 7.2, LaVision 2007
Field of view (data)	430×190 pixels
Interframe time	20 μs
Subset size (final)	12×12
Subset overlap (final)	50 %
Spatial smoothing	5×5 Gaussian smoothing

movement of the bar and clamp introduces dynamic tensile loading on the specimen. At the same time, the high-speed camera is triggered to capture the dynamic deformations at 50 000 fps. The images were analysed by a digital image correlation (DIC) package with the same procedure introduced in the previous work [11]. The imaging and DIC configurations are listed in Table 2; the speckle pattern is formed using spray paint. One of the axial displacement fields obtained from the image analysis is shown in the right-hand side of Fig. 6. As a test material, the same nitrile rubber sheet was used. After inserting this rubber specimen, the width and gauge length are similar to those shown in Fig. 3 left. Three tests were performed with different impact speeds.

The data fields: strain, acceleration and coordinates obtained from the image analysis were applied to the Old (Eq. (3)) and New (Eq. (5)) VFMs in the same way as in the simulation work. One of the VFM analysis results is shown in Fig. 8 left presenting the history of the Young's modulus identifications from the two VFMs. The identification result is similar to the simulation results given in Fig. 4. The identification result of the Old VFM shows the unstable identification instants. Over the first loading period, the two results are almost matched, but after the first unstable identification the two results are not exactly matched; it seems that, after each unstable identification, the Old VFM reaches the similar identification level of the New VFM for only a short period. The reason of this fluctuation can be explained by the averaged acceleration profile (shown in Fig. 8 left). It can be seen that when the averaged acceleration becomes close to zero, i.e. the vicinity of a static stress equilibrium state, the unstable identification starts to occur. When the specimen is in or very close to the equilibrium state, the actual acceleration amplitude can be very low. However, the actual low-amplitude acceleration fields can be obscured by imaging processing noise as the acceleration data used in the VFM are calculated by double differentiation of the displacement data fields, which include imaging noise. When the New VFM, Eq. (5), is used, the virtual work contributed by the acceleration lessens due to the use of the new virtual field, Eq. (4), and instead, the proportion of the virtual work from the traction force is large. Therefore, the effect of unreliable measurements or calculations of the acceleration field at the temporally equilibrium state can be mitigated. This mitigation is the reason for the smooth and stable identification result of the New VFM shown in Fig. 8 left. This result is used to reconstruct the true stress–strain curve by using Eq. (5). The result is plotted in Fig. 8 right; the reconstructed curves from the other two tests are also presented. The legend in this figure provides the strain rate of each test. The stress curves of Test 1 and 2 show the good repeatability of the technique; comparison between Test 1&2 and 3 as well as the quasi-static test indicates that the technique is able to capture the rate dependency of the chosen rubber. The strain rate values given in Fig. 8 right were obtained by

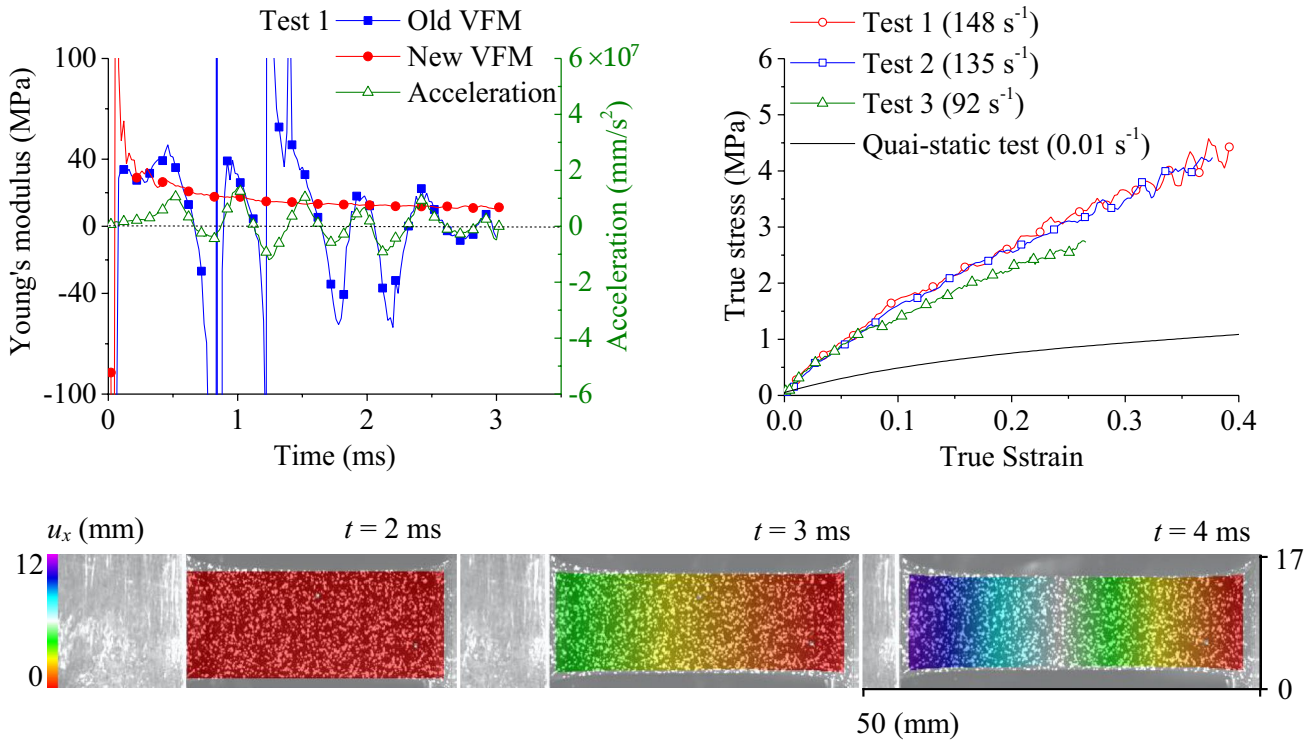

Fig. 8 *Left* Young's modulus identification results of the old (Eq. (2)) and new (Eq. (5)) VFMs applied on the experimental data (Test 1) and the averaged acceleration profile; *right* dynamic true stress–strain curves from Eq. (5); *bottom* dynamic deformation fields in the longitudinal direction at 2, 3 and 4 ms in Test 1

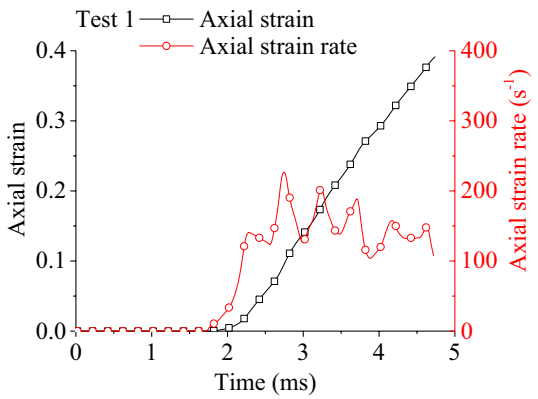

Fig. 9 Axial average strain and strain rate profiles of Test 1 presented in Fig. 1

averaging a strain rate profile of each test. The strain and strain rate profiles of Test 1 are given in Fig. 9.

As shown in Table 2, the stress–strain curves presented in Fig. 8 right were obtained with displacement data which were spatially smoothed by a Gaussian filter of size 5×5. In order to study the effect of the smoothing, several different filter sizes were applied to the same test result of Test 2 given in Fig. 8 right. Five different filter sizes (available in the DIC software) were used, and the smoothed displacement data sets were analysed by the same present VFM. The stress–strain curve results are presented in Fig. 10 left. As can be seen in this figure, the identified stress–strain curves are stable with respect to the given filter sizes. Additionally, the effect of the subset size for the correlation was also studied although 12×12 subset size was the smallest size that produced a low level of random noise. Three additional subset sizes (8×8, 16×16 and 24×24) were applied on the same test data of Test 2. The subset size smaller than 8×8 started to produce de-correlated data. When the sizes larger than 24×24 were used, it was found that the final strain range gradually decreased. Within these limits, it can be seen that the use of the given subset sizes is not significant as shown in Fig. 10 right.

Measurements of Loading and Unloading

When the equipment shown in Fig. 7 was used, it was often found that the incident bar was reflected back smoothly so that it was possible to capture the unloading behaviour of the test sample. In order to regularize this unloading, the apparatus was slightly modified as shown in Fig. 11. On the incident bar, two metal blocks were attached and fixed at given locations, and four rubber

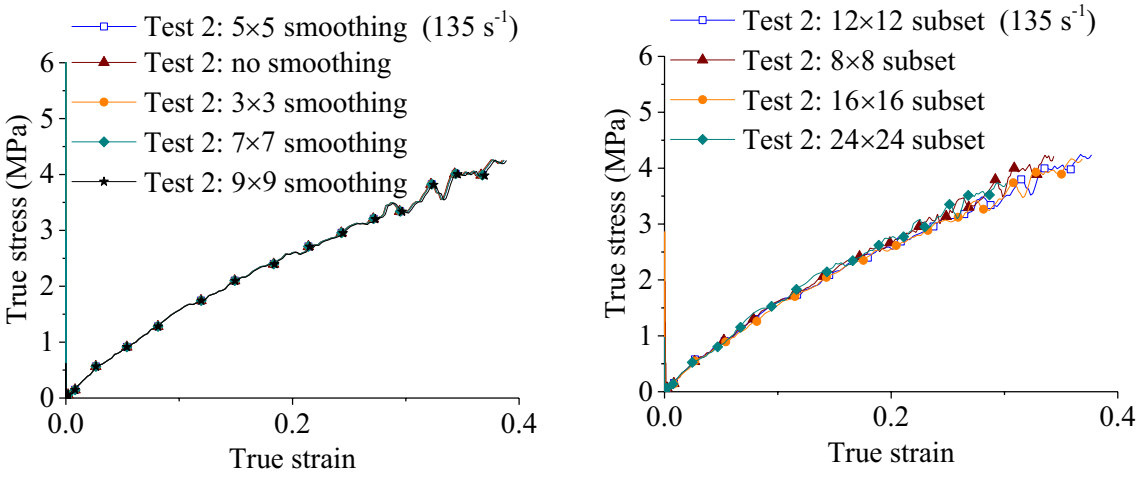

Fig. 10 True stress–strain curves from the test data of Test 2 with (*left*) different smoothing filter and (*right*) subset sizes

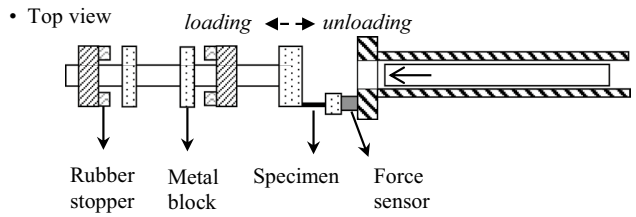

Fig. 11 Schematic representation of the modified dynamic tension test equipment

stoppers were installed respectively on the bar holders as indicated. The location of the left-most metal block determines the final strain of the tensile loading and the one on the right-most side the strain range of the unloading. The loading and unloading directions are also indicated in Fig. 11. The experimental procedure was the same as described above, except that the imaging duration was slightly longer in order to capture the whole loading and unloading deformations. The same New VFM procedure was applied to the imaging data. The true stress–strain curves obtained, including unloading, are presented in Fig. 12 left. This result demonstrates that the use of the present experiment and VFM analysis is able to capture the smooth loading and unloading behaviour under medium strain rate deformation in uniaxial tension. The dashed lines and arrows indicate the range of the average strain rates for each loading and unloading period. Although these average strain rates are provided, the strain rates vary, especially during the unloading period as shown in Fig. 12 right.

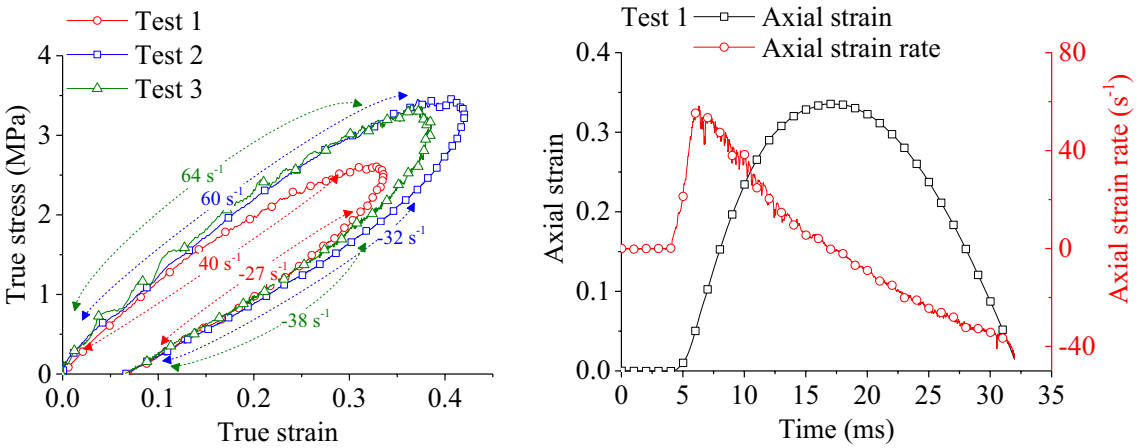

Fig. 12 *Left* True stress–strain curves of the loading and unloading experiments: the numbers and arrows respectively indicate average strain rates and the corresponding ranges; *right* axial average strain and strain rate profiles of Test 1

Conclusions

A new experimental technique is proposed, an improvement to a previously developed VFM analysis and drop-weight test procedure introduced in previous work [11], to characterize the dynamic behaviour of rubbers in uniaxial tension. The previous method utilized the dynamic VFM, in which the principle of virtual work equation is implemented to cancel the traction force term induced from the loaded boundary, so that only acceleration data are used to identify the Young's modulus. One limitation is that although a rubber specimen is continuously deformed in tension, there are stress wave reflections during which the specimen is in an approximate static equilibrium state, where the acceleration field is close to zero, for a short period of time. During this period, the Young's modulus identification is unstable. For this reason, the modulus identification history is discontinuous at the temporary equilibrium instants. In order to overcome this limitation of the previous VFM, a modified VFM was developed in which one of the virtual fields is modified so that the traction, which can be measured at the fixed boundary of a test specimen, is included in the principle of virtual work equation. A new dynamic experimental system was also developed to introduce dynamic loading in tension and simultaneously to measure the traction forces. The test data (full-field and force measurement data) were applied to the new VFM; it is found that the modulus identification is smooth and continuous over the whole loading period. With this advantage of the new VFM result, it is straightforward to reconstruct the true stress–strain curve simply by applying the spatially averaged strain to the modulus identification result. Using this method, a dynamic true stress–strain curve is successfully reconstructed without assuming any particular constitutive model. Furthermore, the experimental apparatus was slightly modified so that the loading and unloading behaviours are captured during dynamic loading.

Using the current experiment system, it is difficult to produce a strain amplitude higher than 0.4 as the specimen deformation takes it out of the imaging area. One way to allow a larger strain would be to use a shorter specimen or a longer distance between the high-speed camera and specimen surface. The first of these methods is well-suited to the new technique, which is able to cope with the increased number of wave oscillations that would result; however, a short specimen may induce complex strain states due to the clamping of the ends. The second method may increase the imaging noise amplitude due to the smaller image resolution. Another possible way to characterize the dynamic behaviour at a larger deformation is to implement the pre-stretching scheme introduced in the previous work [11].

The present VFM can be also extended to include a hyperelastic model within the principle of virtual work equation. Here, the stress–strain curve obtained from the model independent VFM presented here would be used for the evaluation of a suitable constitutive model. Then, the application of this model, with a rate dependent capability, within the VFM formulation would allow further information to be obtained from experiments with varying strain-rate history, as shown, for example, in the unloading experiment. Thus, these experiments have the capability to both identify suitable models, and also to calibrate these models for more complex loading histories that can be evaluated using previously available experimental techniques.

Acknowledgements This material is based upon work supported by the Air Force Office of Scientific Research, Air Force Material Command, USAF under Award Nos. FA8655-12-1-2015 and FA9550-15-1-0448. The U.S Government is authorized to reproduce and distribute reprints for Governmental purpose notwithstanding any copyright notation thereon. The authors thank S Fuller and JL Jordan of AFOSR and M Snyder, J Foley and R Pollak of EOARD for their support. The authors would like to thank R Froud and R Duffin for the construction of the experimental apparatus used in this research, and their helpful advice when designing this apparatus. Finally, we thank Professor F Pierron for his invaluable help with the Virtual Fields Method.

References

1. Field JE, Walley SM, Proud WG et al (2004) Review of experimental techniques for high rate deformation and shock studies. Int J Impact Eng. doi:10.1016/j.ijimpeng.2004.03.005
2. Davidson JS, Fisher JW, Hammons MI et al. (2005) Failure mechanisms of polymer-reinforced concrete masonry walls subjected to blast. J Struct Eng 131:1194–1205. doi:10.1061/(ASCE)0733-9445(2005)131:8(1194)
3. Sarva SS, Deschanel S, Boyce MC, Chen W (2007) Stress–strain behavior of a polyurea and a polyurethane from low to high strain rates. Polymer (Guildf) 48:2208–2213. doi:10.1016/j.polymer.2007.02.058
4. Song B, Chen W (2003) One-dimensional dynamic compressive behavior of EPDM rubber. J Eng Mater Technol 125:294. doi:10.1115/1.1584492
5. Harrigan JJ, Ahonsi B, Palamidi E, Reid SR (2014) Experimental and numerical investigations on the use of polymer Hopkinson pressure bars. Philos Trans A Math Phys Eng Sci 372:20130201. doi:10.1098/rsta.2013.0201
6. Fatt MSH, Bekar I (2004) High-speed testing and material modeling of unfilled styrene butadiene vulcanizates at impact rates. J Mater Sci 39:6885–6899. doi:10.1023/B:JMSC.0000047530.86758.b9
7. Mohotti D, Ali M, Ngo T et al (2014) Strain rate dependent constitutive model for predicting the material behaviour of polyurea under high strain rate tensile loading. Mater Des 53:830–837. doi:10.1016/j.matdes.2013.07.020

8. Niemczura J, Ravi-Chandar K (2011) On the response of rubbers at high strain rates—I. Simple waves. J Mech Phys Solids 59:423–441. doi:10.1016/j.jmps.2010.09.006
9. Chen W, Zhang B, Forrestal MJ (1999) A split Hopkinson bar technique for low-impedance materials. Exp Mech 39:81–85. doi:10.1007/BF02331109
10. Song B, Chen W (2004) Dynamic stress equilibration in split Hopkinson pressure bar tests on soft materials. Exp Mech 44:300–312. doi:10.1007/BF02427897
11. Yoon S, Giannakopoulos I, Siviour CR (2015) Application of the Virtual Fields Method to the uniaxial behavior of rubbers at medium strain rates. Int J Solids Struct 1–16. doi:10.1016/j.ijsolstr.2015.04.017
12. Sutton MA, Orteu J-J, Schreier H (2009) Image correlation for shape, motion and deformation measurements. doi:10.1007/978-0-387-78747-3
13. Pierron F, Grédiac M (2012) The virtual fields method†¯: extracting constitutive mechanical parameters from full-field deformation measurements. Springer, New York
14. Moulart R, Pierron F, Hallett S, Wisnom M (2011) Full-field strain measurement and identification of composites moduli at high strain rate with the virtual fields method. Exp Mech 51:509–536. doi:10.1007/s11340-010-9433-4
15. Kim JH, Lee GA, Lee MG (2015) Determination of dynamic strain hardening parameters using the virtual fields method. Int J Automot Technol 16:145–151. doi:10.1007/s12239-015-0016-3
16. Pierron F, Sutton M a., Tiwari V (2011) Ultra high speed DIC and virtual fields method analysis of a three point bending impact test on an aluminium bar. Exp Mech 51:537–563. doi:10.1007/s11340-010-9402-y
17. Pierron F, Zhu H, Siviour C (2014) Beyond Hopkinson's bar. Philos Trans R Soc A Math Phys Eng Sci 372:20130195. doi:10.1098/rsta.2013.0195
18. Pierron F, Forquin P (2012) Ultra-high-speed full-field deformation measurements on concrete spalling specimens and stiffness identification with the virtual fields method. Strain 48:388–405. doi:10.1111/j.1475-1305.2012.00835.x
19. Ogden RW (1972) Large deformation isotropic elasticity—on the correlation of theory and experiment for incompressible rubberlike solids. Proc R Soc London A Math Phys Sci 326:565–584. doi:10.1098/rspa.1972.0026